Improved sound absorption performance of three-dimensional MPP space sound absorbers by filling with porous materials

Toyoda, Masahiro
Sakagami, Kimihiro
Okano, Mitsuru
Okuzono, Takeshi
Toyoda, Emi

(Citation)
Applied Acoustics,116:311-316

(Issue Date)
2017-01-15

(Resource Type)
journal article

(Version)
Accepted Manuscript

(URL)
https://hdl.handle.net/20.500.14094/90003559

Improved sound absorption performance of three-dimensional MPP space sound absorbers by filling with porous materials

Masahiro Toyoda[a], Kimihiro Sakagami[b], Mitsuru Okano[b], Takeshi Okuzono[b], Emi Toyoda[c]

[a] *Department of Architecture, Faculty of Environmental and Urban Engineering, Kansai University,*
3-3-35, Yamate-cho, Suita-shi, Osaka 564-8680, Japan
[b] *Environmental Acoustics Laboratory, Graduate School of Engineering, Kobe University, Rokko, Nada, Kobe 657-8501 Japan*
[c] *Kobayasi Institute of Physical Research,*
Higashimotomachi, Kokubunji 185-0022, Tokyo, Japan

Abstract

Because microperforated panels (MPPs), which can be made from various materials, provide wide-band sound absorption, they are recognized as one of the next-generation absorption materials. Although MPPs are typically placed in front of rigid walls, MPP space sound absorbers without a backing structure, including three-dimensional cylindrical MPP space absorbers (CMSAs) and rectangular MPP space absorbers (RMSAs), are proposed to extend their design flexibility and easy-to-use properties. On the other hand, improving the absorption performance by filling the back cavity of typical MPP absorbers with porous materials has been shown theoretically, and three-dimensional MPP space absorbers should display similar improvements. Herein the effects of porous materials inserted into the cavities of CMSAs and RMSAs are experimentally investigated and a numerical prediction method using the two-dimensional boundary element method is proposed. Consequently, CMSAs and RMSAs with improved absorption performances are illustrated based on the experimental results, and the applicability of the proposed prediction method as a design tool is confirmed by comparing the experimental and numerical results.

Keywords: sound absorption, MPP, space sound absorber, porous material, BEM

1. Introduction

Microperforated panels (MPPs) are one of the most promising alternatives for next-generation sound absorbers [1, 2, 3, 4]. Typically MPPs are used in conjunction with an air cavity backed by a rigid wall. This setup limits the use of MPPs because MPPs must be professionally installed below ceilings or in front of walls as interior materials.

To offer easy-to-use sound absorption devices using MPPs, the authors have been researching MPP space sound absorbers. First, the sound absorption characteristics of the proposed double-leaf MPP space sound absorber (DLMPP) [5, 6] were examined theoretically and experimentally. However, a DLMPP is a panel-like object with limitations as it is basically set on a floor or hung from a ceiling. If a space sound absorber made of MPPs can be placed more freely, its applications would be diversified. Next, three-dimensional MPP space sound absorbers [CMSA (cylindrical shaped) and RMSA (rectangular shaped)] were proposed [7, 8, 9]. CMSA and RMSA can offer reasonable absorptivities over a rather wider frequency range. Because the sound absorptivity is not very high, herein filling the cavities of CMSA and RMSA with porous materials is investigated.

Porous material in the cavity of typical MPP absorbers has been previously shown to increase the peak and broaden the absorption frequency range [10, 11]. Thus, a similar effect is expected for three-dimensional MPP space sound absorbers. Herein experimental studies on the absorption characteristics of CMSAs and RMSAs filled with porous materials (hereafter referred to as CMSA/RMSA with porous material) are carried out, and a prediction method as a design tool is proposed using the two-dimensional boundary element method.

2. Experiment

2.1. Setup

Because a detailed description of the manufacturing process for CMSA and RMSA specimens is reported elsewhere [7, 9], only the important parameters of the specimens are given here. CMSA specimens with 1- and 2-m

Email address: toyoda@kansai-u.ac.jp (Masahiro Toyoda)

perimeters (318 and 637 mm diameters, respectively) were made of 1-mm-thick polycarbonate MPP. The hole diameter, perforation ratio, and surface density were 0.5 mm, 0.785%, and 1.2 kg/m^2, respectively. RMSA specimens with 1- and 2-m perimeters (squares with 250- and 500-mm sides, respectively) were made of a similar polycarbonate MPP with the same parameters as above except the thickness and surface density were 0.5 mm and 0.6 kg/m^2, respectively. The MPPs were fixed with slim wooden frames. The height of all specimens was 1 m. As the porous material, a 50-mm-thick panels of fiberglass of 32 kg/m^3 were stacked in the cavity. Consequently, the CMSA and RMSA cavities were filled with porous materials. The CMSA/RMSA with porous material described above were placed on the rigid floor of a reverberation chamber (513 m^3 volume and 382 m^2 surface area).

The measurements were performed according to JIS A 1409 [ISO 354 (Ref. [12]) compatible]. In all cases, six specimens were used, and the measurements were carried out with and without a cover (12-mm-thick plywood) on the open top-end. The absorption coefficients were estimated from the measured absorption power divided by the total surface area of the MPPs while ignoring the area of the top-ends. Figure 1 shows a picture of the experimental setup.

2.2. Results

Figures 2 (1-m perimeter) and 3 (2-m perimeter) compare the measured results for CMSA with porous material to those without a porous material inside [7]. In addition, the cases with and without a cover on the open top-end are shown. The absorptivity greatly increases due to the effect of a porous material inside. The effect is especially significant around the peak frequency, but gradually becomes smaller as the frequency increases. In the 2-m perimeter case, the absorption peak becomes higher upon inserting a porous material. It is inferred that the absorption peak is due to the resonance inside the cavity because the peak frequency is lower than that of the 1-m perimeter case and the bandwidth of absorption is extended by the decrease of the acoustical stiffness of the cavity due to its bigger volume. The maximum absorption coefficient exceeds 1.0 due to the area effect [13], demonstrating that CMSA with porous material is far more efficient as a sound absorber. The impact of the cover on the top-end is observed around and above the peak frequencies; the absorption coefficients of CMSAs without covers are larger than those with covers. This is because the top-end area

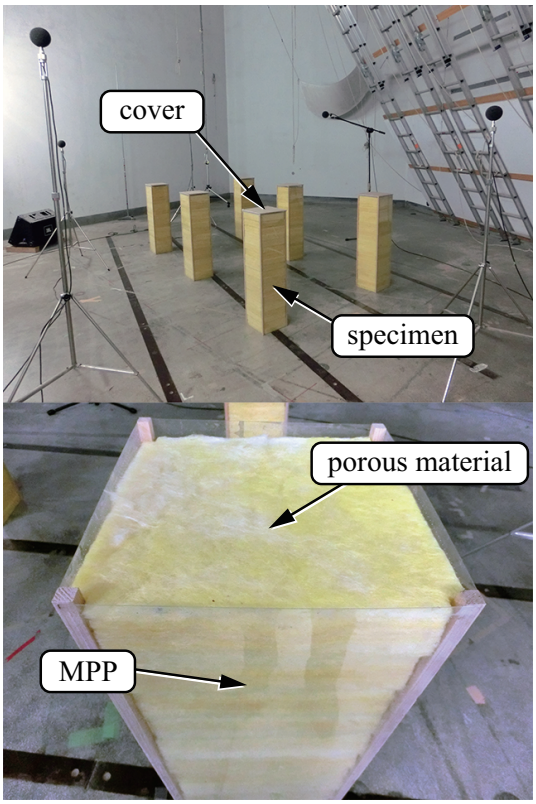

Figure 1: Example of the experimental set-up for 1-m perimeter RMSAs filled with a porous material in the reverberation chamber. The arrangement of RMSAs with covers and the close-up of an RMSA without a cover are shown in upper and lower pictures, respectively.

relative to the entire surface area in the 2-m perimeter case is larger than that in a 1-m perimeter case, where the surface of the porous material itself is exposed to air without covers. Hence, the effect of a cover can be ignored when the perimeter is sufficiently small.

Figures 4 (1-m perimeter) and 5 (2-m perimeter) compare the results for RMSA with porous material to those without porous material inside [9]. Additionally, the cases with and without a cover on the open top-end are compared. The same tendencies as CMSA with porous material cases are observed. The effect of the porous material inside is significant, and the influence of the cover, which is stronger in the 2-m perimeter case, is observed

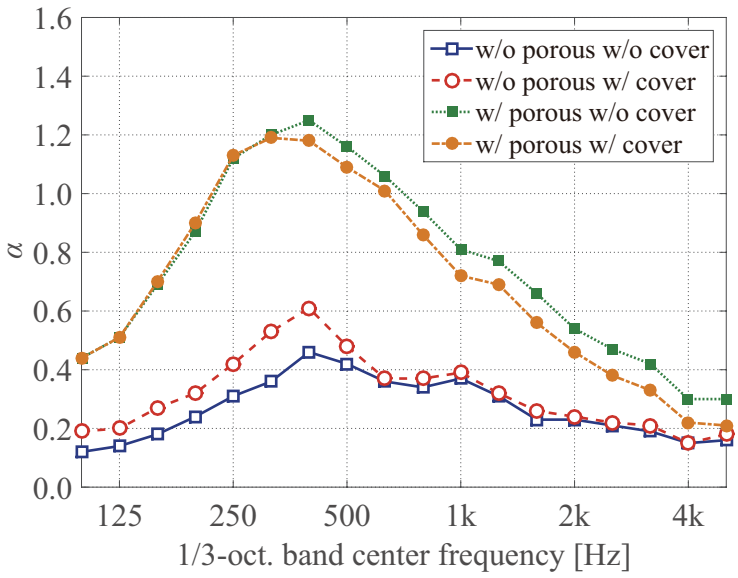

Figure 2: Comparison of the experimental results for 1-m perimeter CMSA with and without a porous material.

around and above the peak frequencies.

3. Prediction

3.1. Formulation

3.1.1. Model

A three-dimensional calculation model should be considered when dealing with CMSAs and RMSAs. However, the total dissipated energy of CMSAs and RMSAs under a random incidence is determined due mostly to the normal incidence rather than the oblique incidence of elevation. Consequently, two-dimensional numerical analyses can provide sufficient predictions for the absorption characteristics of CMSAs and RMSAs [8]. Thus, a similar two-dimensional formulation is employed here, drastically reducing the required computational resources. Figure 6 shows the two-dimensional calculation models of CMSA/RMSA with porous material, assuming an incident plane wave with a unit amplitude and incident azimuth angle θ.

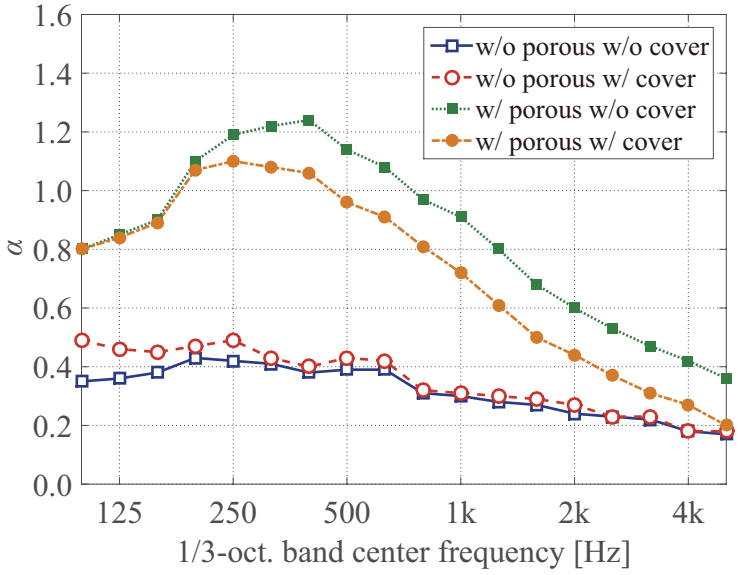

Figure 3: Comparison of the experimental results for 2-m perimeter CMSA with and without a porous material.

3.1.2. Boundary integral equation

As shown in Fig. 7, region Ω_1 is bounded externally by Σ of center p, which is the sound receiver, and internally by Γ. Small spheres σ_s and σ_p have respective centers s and p and small radii ϵ, where s is the sound source, q is a point on the boundary, and $\mathbf{n}$ is the inward normal vector. Transmission admittance ratio A is assumed on Γ. Region Ω_2 is bounded externally by Γ. The time factor $\exp(-\mathrm{i}\omega t)$ is suppressed throughout, where i is an imaginary unit, ω is the angular frequency, and t is time. Green's identity or integration by parts can be applied to region Ω_1 as

$$\int_{\Omega_1} \left(f\nabla^2 g - g\nabla^2 f\right) dS = \int_{\Sigma+\sigma_\mathrm{s}+\sigma_\mathrm{p}+\Gamma} \left(f\frac{\partial g}{\partial \mathbf{n}} - \frac{\partial f}{\partial \mathbf{n}} g\right) dL, \tag{1}$$

where f and g are continuous and smooth functions. Substituting velocity potential Φ_1 and basic solution G_1, which satisfy the two-dimensional Helmholtz equation, for f and g, respectively, yields the boundary integral equation for region Ω_1. Basic solution G_1 can be written as

$$G_1(\mathbf{r}_\mathrm{p}, \mathbf{r}_\mathrm{q}) = \frac{\mathrm{i}}{4}\mathbf{H}_0^{(1)}(k_1 r_\mathrm{pq}) = \frac{\mathrm{i}}{4}\left\{\mathbf{J}_0(k_1 r_\mathrm{pq}) + \mathrm{i}\mathbf{Y}_0(k_1 r_\mathrm{pq})\right\}, \tag{2}$$

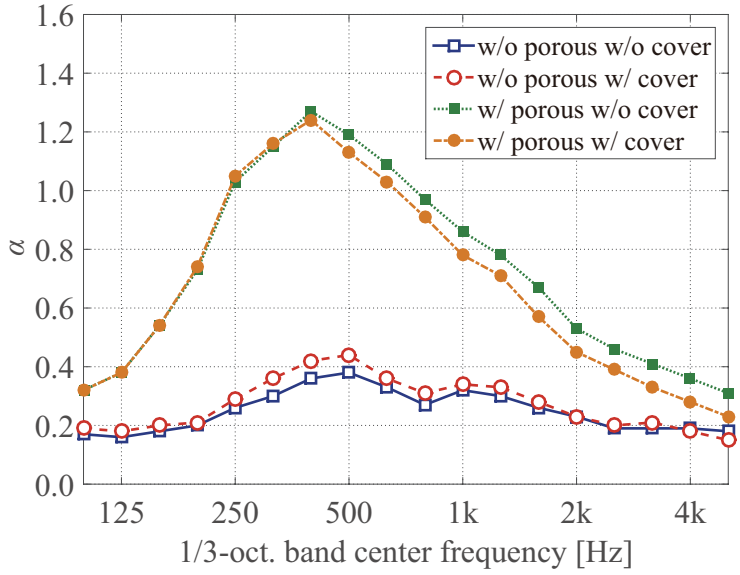

Figure 4: Comparison of the experimental results for 1-m perimeter RMSA with and without a porous material.

where $\mathbf{r}$ is a position vector, k_1 is the complex wavenumber of the medium in Ω_1, and r_{pq} is the distance between p and q. Note that, when Ω_1 is filled with air, k_1 is equal to real number k_0 which is the wavenumber of air. $\mathbf{H}_0^{(1)}$, $\mathbf{J}_0$, and $\mathbf{Y}_0$ are the Hankel function of the first kind of order zero, the Bessel function of order zero, and Neumann function of order zero, respectively. Taking the limit $\epsilon \to 0$, the integral over σ_{s} in Eq. (1) can be written as

$$\int_{\sigma_{\mathrm{s}}} \left\{ \Phi_1(\mathbf{r}_{\mathrm{q}}) \frac{\partial G_1(\mathbf{r}_{\mathrm{p}}, \mathbf{r}_{\mathrm{q}})}{\partial \mathbf{n}_{\mathrm{q}}} - \frac{\partial \Phi_1(\mathbf{r}_{\mathrm{q}})}{\partial \mathbf{n}_{\mathrm{q}}} G_1(\mathbf{r}_{\mathrm{p}}, \mathbf{r}_{\mathrm{q}}) \right\} dL = \phi_{\mathrm{d}}(\mathbf{r}_{\mathrm{p}}), \tag{3}$$

where ϕ_{d} is the velocity potential due to the direct wave from the sound source. Similarly, the integral over σ_{p} in Eq. (1) can be expressed as

$$\int_{\sigma_{\mathrm{p}}} \left\{ \Phi_1(\mathbf{r}_{\mathrm{q}}) \frac{\partial G_1(\mathbf{r}_{\mathrm{p}}, \mathbf{r}_{\mathrm{q}})}{\partial \mathbf{n}_{\mathrm{q}}} - \frac{\partial \Phi_1(\mathbf{r}_{\mathrm{q}})}{\partial \mathbf{n}_{\mathrm{q}}} G_1(\mathbf{r}_{\mathrm{p}}, \mathbf{r}_{\mathrm{q}}) \right\} dL = -C(\mathbf{r}_{\mathrm{p}}) \Phi_1(\mathbf{r}_{\mathrm{p}}), \tag{4}$$

where $C(\mathbf{r}_{\mathrm{q}})$ is the ratio of the included-part solid angle of σ_{p} in Ω_1 to 4π; if p is on a smooth boundary, $C(\mathbf{r}_{\mathrm{q}}) = 1/2$. Assuming that Σ is a circle with

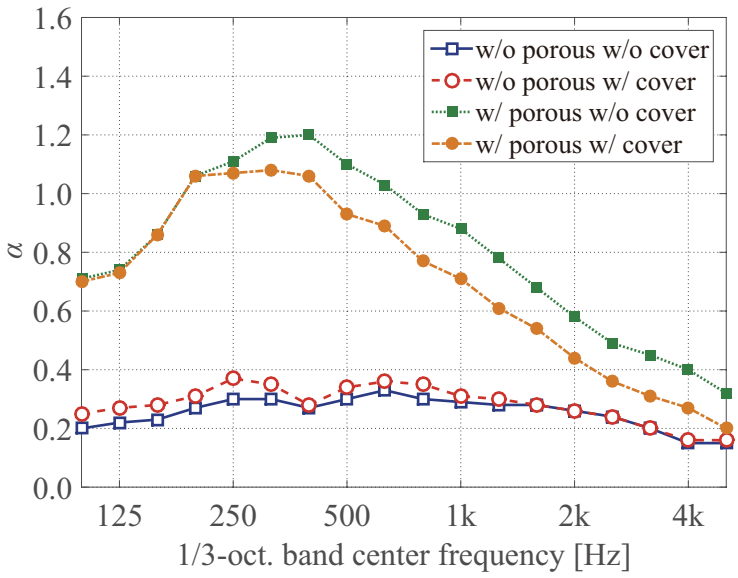

Figure 5: Comparison of the experimental results for 2-m perimeter RMSA with and without a porous material.

an infinite radius and considering the Sommerfeld radiation condition [14], which can be expressed as

$$|r_{\mathrm{pq}}\Phi_1(\mathbf{r}_{\mathrm{q}})| < K, \quad \sqrt{r_{\mathrm{pq}}}\left\{\frac{\partial\Phi_1(\mathbf{r}_{\mathrm{q}})}{\partial r_{\mathrm{pq}}} - \mathrm{i}k_1\Phi_1(\mathbf{r}_{\mathrm{q}})\right\} \to 0 \quad (r_{\mathrm{pq}} \to \infty)\,, \tag{5}$$

where K is a finite real number, the integral over Σ in Eq. (1) can be neglected. Consequently, substituting Eqs. (3) and (4) into Eq. (1) yields

$$\phi_{\mathrm{d}}(\mathbf{r}_{\mathrm{p}}) + \int_\Gamma \left\{\phi_1(\mathbf{r}_{\mathrm{q}})\frac{\partial G_1(\mathbf{r}_{\mathrm{p}},\mathbf{r}_{\mathrm{q}})}{\partial \mathbf{n}_{\mathrm{q}}} - \frac{\partial\phi_1(\mathbf{r}_{\mathrm{q}})}{\partial \mathbf{n}_{\mathrm{q}}}G_1(\mathbf{r}_{\mathrm{p}},\mathbf{r}_{\mathrm{q}})\right\} dL = \frac{1}{2}\phi_1(\mathbf{r}_{\mathrm{p}}) \quad (\mathrm{p} \in \Gamma)\,, \tag{6}$$

where ϕ_1 is the velocity potential on Γ of the Ω_1 side. Similarly, the boundary integral equation for region Ω_2 can be obtained as

$$-\int_\Gamma \left\{\phi_2(\mathbf{r}_{\mathrm{q}})\frac{\partial G_2(\mathbf{r}_{\mathrm{p}},\mathbf{r}_{\mathrm{q}})}{\partial \mathbf{n}_{\mathrm{q}}} - \frac{\partial\phi_2(\mathbf{r}_{\mathrm{q}})}{\partial \mathbf{n}_{\mathrm{q}}}G_2(\mathbf{r}_{\mathrm{p}},\mathbf{r}_{\mathrm{q}})\right\} dL = \frac{1}{2}\phi_2(\mathbf{r}_{\mathrm{p}}) \quad (\mathrm{p} \in \Gamma)\,, \tag{7}$$

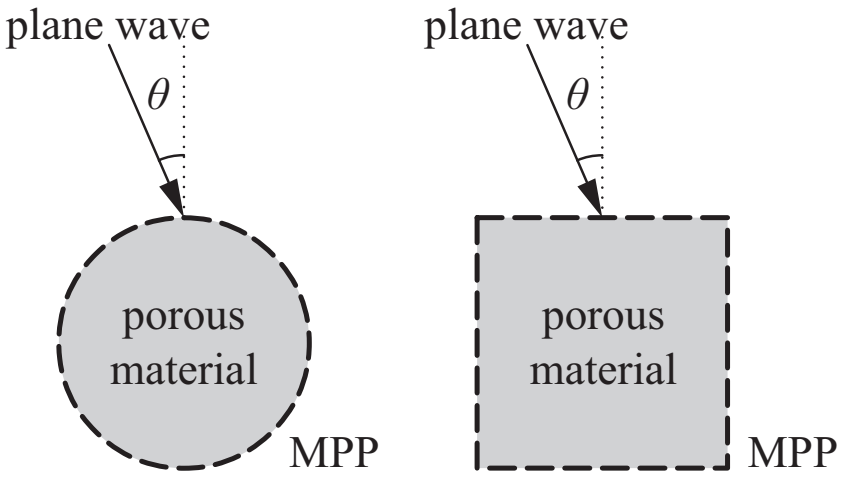

Figure 6: Two-dimensional models of CMSA and RMSA filled with porous materials.

where ϕ_2 is the velocity potential on Γ of the Ω_2 side. G_2 is the basic solution expressed as

$$G_2(\mathbf{r}_\mathrm{p}, \mathbf{r}_\mathrm{q}) = \frac{\mathrm{i}}{4}\mathbf{H}_0^{(1)}(k_2 r_\mathrm{pq}) = \frac{\mathrm{i}}{4}\left\{\mathbf{J}_0(k_2 r_\mathrm{pq}) + \mathrm{i}\mathbf{Y}_0(k_2 r_\mathrm{pq})\right\}, \tag{8}$$

where k_2 is the complex wavenumber of medium in Ω_2.

Let $v(\mathbf{r}_\mathrm{q})$ be the particle velocity at q, $p_{1,2}(\mathbf{r}_\mathrm{q})$ be the sound pressures on Γ of the $\Omega_{1,2}$ sides at q, and $\rho_{1,2}$ be the complex densities of the media in $\Omega_{1,2}$. Then

$$\begin{aligned}
\frac{\partial\phi_1(\mathbf{r}_\mathrm{q})}{\partial\mathbf{n}_\mathrm{q}} = \frac{\partial\phi_2(\mathbf{r}_\mathrm{q})}{\partial\mathbf{n}_\mathrm{q}} &= -v(\mathbf{r}_\mathrm{q}) \\
&= \frac{A}{\rho_0 c_0}(p_1(\mathbf{r}_\mathrm{q}) - p_2(\mathbf{r}_\mathrm{q})) \\
&= -\mathrm{i}k_0\left(\frac{\rho_1}{\rho_0}A\phi_1 - \frac{\rho_2}{\rho_0}A\phi_2\right),
\end{aligned} \tag{9}$$

where ρ_0 and c_0 are the density and soundspeed of air, respectively. Note that ρ_1 is equal to a real number ρ_0 when Ω_1 is filled with air. Substituting Eq. (9) into Eqs. (6) and (7) yields the boundary integral equations for Ω_1 and Ω_2, which are written by

$$\frac{1}{2}\phi_1(\mathbf{r}_\mathrm{p}) - \int_\Gamma \phi_1(\mathbf{r}_\mathrm{q})\frac{\partial G_1(\mathbf{r}_\mathrm{p}, \mathbf{r}_\mathrm{q})}{\partial\mathbf{n}_\mathrm{q}}dL - \mathrm{i}k_0\frac{\rho_1}{\rho_0}\int_\Gamma A\phi_1(\mathbf{r}_\mathrm{q})G_1(\mathbf{r}_\mathrm{p}, \mathbf{r}_\mathrm{q})dL$$

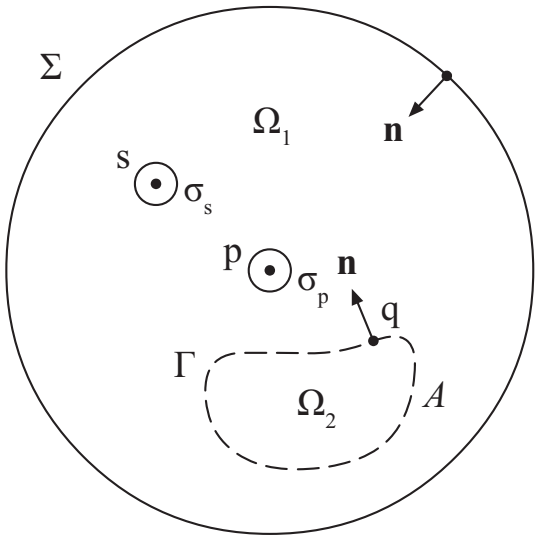

Figure 7: Two-dimensional model to derive the boundary integral equation.

$$+\mathrm{i}k_0\frac{\rho_2}{\rho_0}\int_\Gamma A\phi_2(\mathbf{r}_\mathrm{q})G_1(\mathbf{r}_\mathrm{p},\mathbf{r}_\mathrm{q})dL=\phi_\mathrm{d}(\mathbf{r}_\mathrm{p}), \tag{10}$$

$$\frac{1}{2}\phi_2(\mathbf{r}_\mathrm{p})+\int_\Gamma \phi_2(\mathbf{r}_\mathrm{q})\frac{\partial G_2(\mathbf{r}_\mathrm{p},\mathbf{r}_\mathrm{q})}{\partial \mathbf{n}_\mathrm{q}}dL+\mathrm{i}k_0\frac{\rho_1}{\rho_0}\int_\Gamma A\phi_1(\mathbf{r}_\mathrm{q})G_2(\mathbf{r}_\mathrm{p},\mathbf{r}_\mathrm{q})dL$$
$$-\mathrm{i}k_0\frac{\rho_2}{\rho_0}\int_\Gamma A\phi_2(\mathbf{r}_\mathrm{q})G_2(\mathbf{r}_\mathrm{p},\mathbf{r}_\mathrm{q})dL=0. \tag{11}$$

Discretizing Γ with N constant elements, Eqs. (10) and (11) can be approximately rewritten as

$$\frac{1}{2}\phi_{1i}-\sum_{j=1}^{N}\phi_{1j}\int_{\Gamma_j}\frac{\partial G_1(\mathbf{r}_i,\mathbf{r}_\mathrm{q})}{\partial \mathbf{n}_\mathrm{q}}dL-\mathrm{i}k_0\frac{\rho_1}{\rho_0}\sum_{j=1}^{N}A_j\phi_{1j}\int_{\Gamma_j}G_1(\mathbf{r}_i,\mathbf{r}_\mathrm{q})dL$$
$$+\mathrm{i}k_0\frac{\rho_2}{\rho_0}\sum_{j=1}^{N}A_j\phi_{2j}\int_{\Gamma_j}G_2(\mathbf{r}_i,\mathbf{r}_\mathrm{q})dL=\phi_{\mathrm{d},i}\ \ (i=1,\cdots,N), \tag{12}$$

$$\frac{1}{2}\phi_{2i}+\sum_{j=1}^{N}\phi_{2j}\int_{\Gamma_j}\frac{\partial G_2(\mathbf{r}_i,\mathbf{r}_\mathrm{q})}{\partial \mathbf{n}_\mathrm{q}}dL+\mathrm{i}k_0\frac{\rho_1}{\rho_0}\sum_{j=1}^{N}A_j\phi_{1j}\int_{\Gamma_j}G_2(\mathbf{r}_i,\mathbf{r}_\mathrm{q})dL$$
$$-\mathrm{i}k_0\frac{\rho_2}{\rho_0}\sum_{j=1}^{N}A_j\phi_{2j}\int_{\Gamma_j}G_2(\mathbf{r}_i,\mathbf{r}_\mathrm{q})dL=0\ \ (i=1,\cdots,N). \tag{13}$$

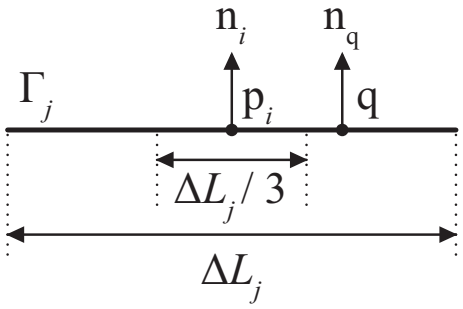

Figure 8: Region where the singular kernel is estimated by Eq. (16).

where

$$\phi_{\mathrm{d},i} = e^{\mathrm{i}k\{\mathbf{h}(\theta)\cdot\mathbf{r}_i\}}, \tag{14}$$

$$\frac{\partial G_{1,2}(\mathbf{r}_i,\mathbf{r}_\mathrm{q})}{\partial \mathbf{n}_\mathrm{q}} = -\frac{\mathrm{i}k_{1,2}}{4}\mathbf{H}_1^{(1)}(k_{1,2}r_{\mathrm{p}_i\mathrm{q}})\cos(\mathbf{n}_i,\mathbf{n}_\mathrm{q}). \tag{15}$$

$\mathbf{h}(\theta) = (\sin\theta, -\cos\theta)$ in Eq. (14) is a unit vector indicating the direction of the plane wave and p_i in Eq. (15) is the center of ith element. Potentials ϕ_{1i} and ϕ_{2i} can be obtained by solving simultaneous equations of Eqs. (12) and (13). In Eqs. (12) and (13), the fourth-order Gauss-Legendre quadrature is employed to calculate the integrals of Eqs. (2), (8), and (15) for $i \neq j$. For $i = j$, the intgral of Eq. (15) becomes zero and the integrals of Eqs. (2) and (8), which has singularity, is estimated for a region of length $\Delta L_j/3$ of center p_i (Fig. 8) as

$$\begin{aligned} 2\int_0^{\Delta L_j/6} \frac{\mathrm{i}}{4}\mathbf{H}_0^{(1)}(k_{1,2}r)dr &\approx 2\int_0^{\Delta L_j/6} \frac{\mathrm{i}}{4}\cdot\frac{2\mathrm{i}}{\pi}\log(k_{1,2}r)dr \\ &= -\frac{\Delta L_j}{6\pi}\left\{\log\left(\frac{k_{1,2}\Delta L_j}{6}\right) - 1\right\}, \end{aligned} \tag{16}$$

where ΔL_j denotes the length of jth element. The integrals for the other regions are estimated using the Gauss-Legendre quadrature. Transmission admittance ratio A_j in Eqs. (12) and (13) is given by Maa's theory [1].

3.1.3. Dissipated energy ratio

The sound absorption performance of CMSA/RMSA with porous material should be evaluated by the energy dissipated in the structure. As for

space sound absorbers such as CMSA/RMSA with porous material, parts of the incident energy are reflected, transmitted, and dissipated by the MPP and porous material. Therefore the dissipated energy ratio is equivalent to the difference in the absorption and transmission coefficients, $\alpha - \tau$. Hereafter this difference in coefficients is used to discuss the sound absorption performance. The average value of $\alpha - \tau$ over all incident angles corresponds to the diffuse sound absorption coefficient measured in a reverberation chamber [15]. In the structures, both MPPs and porous materials can dissipate sound energy. Therefore, the total dissipated energy can be evaluated by the net energy through the outside surface of MPPs. The net energy through the jth element under a plane wave of incident angle θ is expressed as

$$W_j(\theta) = \frac{1}{2}\mathrm{Re}\left\{p_j \cdot (-v_j)^*\right\} \Delta L_j, \tag{17}$$

where the asterisk denotes the complex conjugate. p_j is the sound pressure on Γ of the Ω_1 side, which is expressed as

$$p_j = \rho_1 \frac{\partial \phi_{1j}}{\partial t} = -\mathrm{i}\rho_1 \omega \phi_{1j}. \tag{18}$$

According to Eq. (9), v_j is expressed as

$$v_j = \mathrm{i}k_0 \left(\frac{\rho_1}{\rho_0} A_j \phi_{1j} - \frac{\rho_2}{\rho_0} A_j \phi_{2j} \right). \tag{19}$$

Then the total dissipated energy can be rewritten as

$$W_\mathrm{a}(\theta) = \sum_{j=1}^{N} W_j(\theta) = \frac{(\rho_0 \omega)^2}{2\rho_0 c_0} \frac{1}{\rho_0^2} \sum_{j=1}^{N} \mathrm{Re}\left[A_j^* \left\{ |\rho_1 \phi_{1j}|^2 - \rho_1 \phi_{1j} \left(\rho_2 \phi_{2j}\right)^* \right\} \right] \Delta L_j. \tag{20}$$

Next the incident energy into a CMSA can be given by

$$W_\mathrm{in}(\theta) = \frac{(\rho_0 \omega)^2}{2\rho_0 c_0} \frac{l_1}{\pi}, \tag{21}$$

where l_1 is the perimeter of the circle. On the other hand, the incident energy into an RMSA can be written as

$$W_\mathrm{in}(\theta) = \frac{(\rho_0 \omega)^2}{2\rho_0 c_0} l_2 \left(\cos\theta + \sin\theta\right), \tag{22}$$

where l_2 is the side length of the square. Consequently, considering the symmetric property of a CMSA, the dissipated energy ratio of a CMSA with porous material can be expressed as

$$\alpha - \tau = \frac{W_{\mathrm{a}}(\theta)}{W_{\mathrm{in}}(\theta)} = \frac{\pi}{\rho_0^2 l_1} \sum_j \mathrm{Re}\left[A_j^* \left\{|\rho_1\phi_{1j}|^2 - \rho_1\phi_{1j}(\rho_2\phi_{2j})^*\right\}\right] \Delta L_j, \quad (23)$$

while that of a RMSA with porous material can be written as

$$\alpha-\tau = \frac{\displaystyle\int_0^{\pi/4} W_{\mathrm{a}}(\theta)d\theta}{\displaystyle\int_0^{\pi/4} W_{\mathrm{in}}(\theta)d\theta} = \frac{\displaystyle\int_0^{\pi/4} \sum_j \mathrm{Re}\left[A_j^* \left\{|\rho_1\phi_{1j}|^2 - \rho_1\phi_{1j}(\rho_2\phi_{2j})^*\right\}\right] \Delta L_j d\theta}{\rho_0^2 l_2 \displaystyle\int_0^{\pi/4} (\cos\theta + \sin\theta)\, d\theta}. \quad (24)$$

3.2. Numerical examples and discussions

Figure 9 shows the numerical results of the energy dissipation ratio for a CMSA with porous material of 10,000-Ns/m^4 flow resistivity with a 1-m perimeter and the experimental results of absorption coefficient, which is shown in Fig. 2. The value of flow resistivity used in the calculation was determined considering the potential range of flow resistivity for 32 kg/m^3 glass wool [16]. No significant difference cannot be found between the results for the least and most flow resistivity of the range. The MPP parameters are the same as those described in Sec. 2.1. In the numerical analyses, the complex density and the basic solution for the porous material are calculated using Miki's experimental formula [17]. The numerical results predict the general tendency of the experimental ones fairly well including the area effect [18], but the discrepancies are somewhat large above 400 Hz; the maximum difference is about 0.3. These discrepancies are attributed to the effects of the bending stiffness of an MPP, which is not taken into account in the theoretical formulation, the manufacturing accuracy of the experimental samples, and three-dimensional effects such as the oblique incidence of elevation. Figure 10 shows the numerical results of the energy dissipation ratio for a CMSA with porous material with a 2-m perimeter and the experimental results of absorption coefficient, which is shown in Fig. 3. The MPP parameters are the same as those of CMSA with 1-m perimeter. The peak frequency of the experimental results is lower than that of the 1-m perimeter case. This trend can also be seen in the predicted results, but the discrepancies are larger than

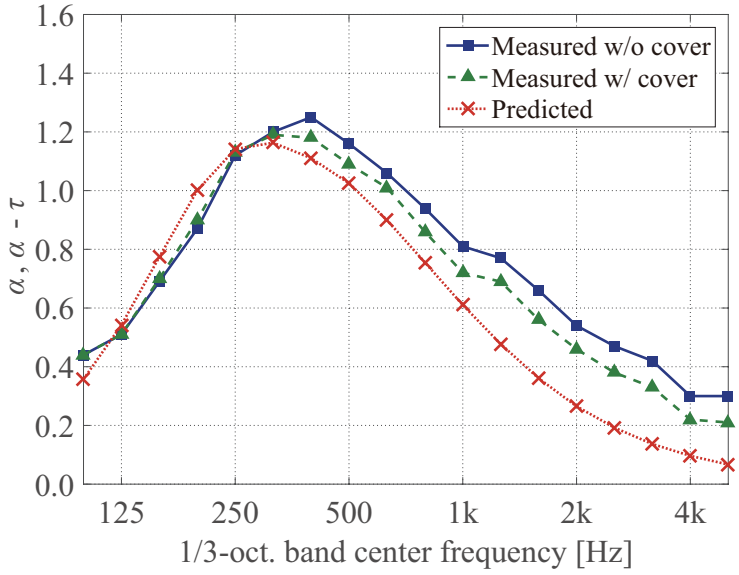

Figure 9: Comparison between the measured and the predicted results for CMSA filled with a porous material (1-m perimeter).

those of the 1-m perimeter case. This is because a larger perimeter with the same height of experimental samples yields a larger difference between the experimental three-dimensional shape and analytical two-dimensional model [8]. That is, the two-dimensional analysis treats an infinitely long CMSA with porous material. Therefore, the accuracy of the proposed two-dimensional method depends on the ratio of the perimeter to the height of the experimental samples.

Next, Fig. 11 shows the numerical results of the energy dissipation ratio for an RMSA filled with a porous material of 10,000-Ns/m^4 flow resistivity with a 1-m perimeter and the experimental results of absorption coefficient, which is shown in Fig. 4. The MPP parameters are the same as those described in Sec. 2.1. The trend of the absorption characteristics is similar to that of the CMSA case. However, the prediction accuracy exceeds that for a CMSA despite the fact that the numerical analysis does not consider the wooden frame used in the experiment. The better accuracy may be due to the thinner MPP, which offers a smaller bending stiffness as well as a precise and easy manufacturing process to realize RMSA. Figure 12 compares the

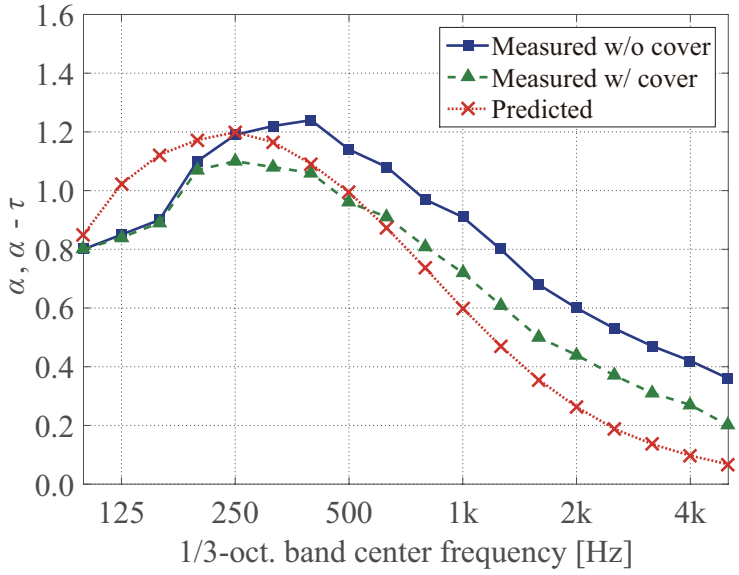

Figure 10: Comparison between the measured and the predicted results for CMSA filled with a porous material (2-m perimeter).

2-m perimeter case. Although some discrepancies are attributed to the ratio of the perimeter to the height in the experimental samples, the total discrepancies are smaller than those in the CMSA case due to the same reason as the 1-m perimeter case.

Finally the numerical results of CMSA/RMSA with porous material are compared for 1-m and 2-m perimeters (Fig. 13), which are filled with a porous material of 10,000-Ns/m^4 flow resistivity. The thickness of MPP, hole diameter, perforation ratio, and surface density are 0.4 mm, 0.4 mm, 0.8%, and 0.5 kg/m^2, respectively. Although the difference due to the cross-sectional shape is rather small when the perimeters are the same, CMSA shows a slightly higher absorption. This result implies that a cylindrical cross-sectional shape is more effective than a convex polygonal shape.

4. Conclusions

As an attempt to improve the absorption performance of three-dimensional MPP space absorbers (CMSA and RMSA), the authors propose CMSAs and

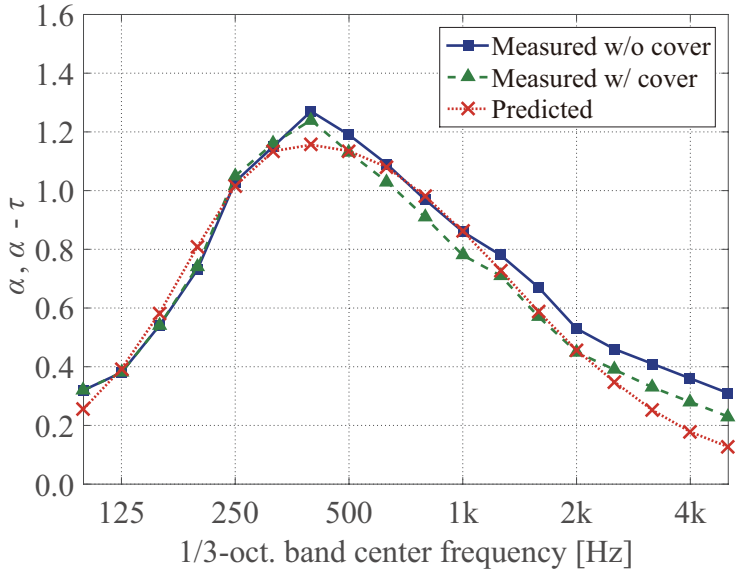

Figure 11: Comparison between the measured and the predicted results for RMSA filled with a porous material (1-m perimeter).

RMSAs filled with porous materials. As expected, the absorption performance is greatly improved in the experimental studies involving porous materials in the cavity; the peak is more significant for CMSA than RMSA. Additionally, the absorption band width becomes much wider.

Furthermore, the prediction method as a design tool of CMSA/RMSA with porous material is proposed using the two-dimensional boundary element method. Although some discrepancies between the experimental and numerical results can be observed, the prediction trend is fairly accurate, confirming the applicability of the method as a design tool. However, three-dimensional analysis is necessary for more accurate predictions because the accuracy of the two-dimensional analysis can be insufficient for CMSA/RMSA with a large perimeter.

References

[1] Maa DY. Theory and design of microperforated panel sound-absorbing constructions. Scientia Sinica 1975; 17: 55–71.

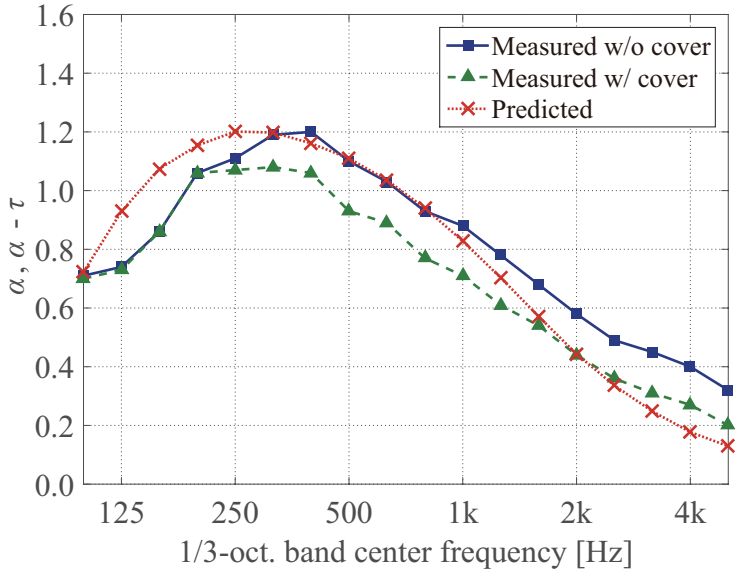

Figure 12: Comparison between the measured and the predicted results for RMSA filled with a porous material (2-m perimeter).

[2] Maa DY. Microperforated-panel wideband absorber. Noise Control Eng J 1987; 29: 77–84.

[3] Maa DY. Potential of microperforated panel absorber. J Acoust Soc Am 1998; 104: 2861–2866.

[4] Maa DY. Practical single MPP absorber. Int J Acoust Vib 2007; 12: 3–6.

[5] Sakagami K, Morimoto M, Koike W. A numerical study of double-leaf microperforated panel absorbers. Appl Acoust 2006; 67: 609–619.

[6] Sakagami K, Nakamori T, Morimoto M, Yairi M. Double-leaf microperforated panel space absorbers: A revised theory and analysis. Appl Acoust 2009; 70: 703–709.

[7] Sakagami K, Oshitani T, Yairi M, Toyoda E, Morimoto M. An experimental study on a cylindrical microperforated panel space sound absorber. Noise Control Eng J 2012; 60: 22–28.

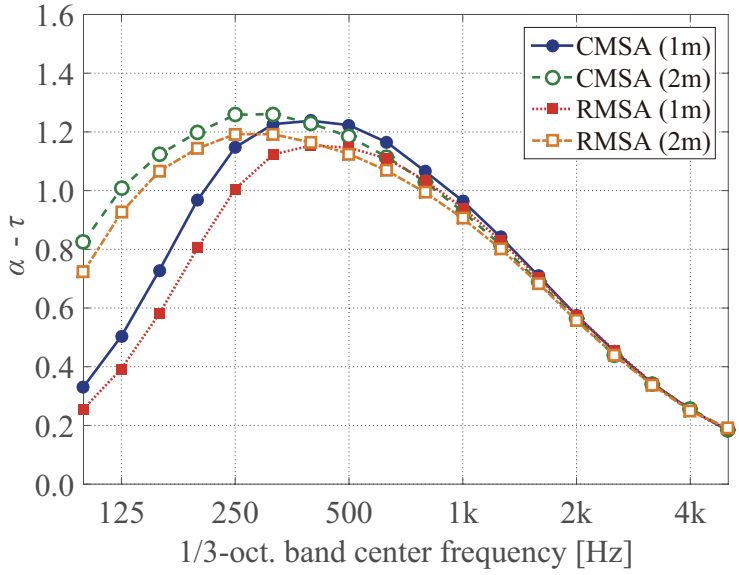

Figure 13: Comparison between the predicted results for CMSA and RMSA filled with a porous material.

[8] Toyoda M, Kobatake S, Sakagami K. Numerical analyses of the sound absorption of three-dimensional MPP space sound absorbers. Appl Acoust 2014; 79: 69–74.

[9] Sakagami K, Yairi M, Toyoda E, Toyoda M. An experimental study of the sound absorption of three-dimensional MPP space sound absorbers: rectangular MPP space sound absorber (RMSA). Acoust Australia 2013; 41: 156–159.

[10] Sakagami K, Kobatake S, Kano K, Morimoto M, Yairi M. Sound absorption characteristics of a single microperforated panel absorber backed by a porous absorbent layer. Acoust Australia 2011; 39: 95–100.

[11] Okano M, Sakagami K, Yairi M. Effect of a porous absorbing layer on absorption characteristics of a double-leaf MPP space sound absorber. Memoirs of the Grad. Sch. of Eng. and System Informatics, Kobe Univ. 2014; 6: 7–12.

[12] ISO 354:2003: Acoustics - Measurement of sound absorption in a rever-

beration room (International Organization for Standardization, Geneva, Switzerland).

[13] Maekawa Z, Rindel JH, Lord P. Environmental and Architectural Acoustics 2nd edition. Oxon: Spon Press; 2011.

[14] Baker BB, Copson ET. The mathematical theory of Huygens principle 3rd edition. New York: Chelsea; 1987.

[15] Sakagami K, Uyama T, Morimoto M, Kiyama M. Prediction of the reverberation absorption coefficient of finite-size membrane absorbers. Appl Acoust 2005; 66: 653–668.

[16] Tarnow V. Measured anisotropic air flow resistivity and sound attenuation of glass wool, J Acoust Soc Am 2002; 111: 2735-2739.

[17] Miki Y. Acoustical properties of porous mateirlas –Modifications of Delany-Bazley models–. J Acoust Soc Jpn (E) 1990; 11: 19–24.

[18] Kawai Y, Meotoiwa H. Estimation of the area effect of sound absorbent surfaces by using a boundary integral equation. Acoust Sci Tech 2005; 26: 123–127.